Speed Control of a Six-Phase IM Fed by a Multi-Modular Matrix Converter Using an Inner PTC With Reduced Computational Burden

EDGAR MAQUEDA[1], SERGIO TOLEDO[1], (Member, IEEE), DAVID CABALLERO[1], FEDERICO GAVILAN[1], JORGE RODAS[1], (Senior Member, IEEE), MAGNO AYALA[1], LARIZZA DELORME[1], (Student Member, IEEE), RAUL GREGOR[1], AND MARCO RIVERA[2], (Senior Member, IEEE)

[1]Laboratory of Power and Control Systems, Facultad de Ingeniería, Universidad Nacional de Asunción, Luque 2060, Paraguay
[2]Department of Electrical Engineering, Universidad de Talca, Curicó 3341717, Chile

Corresponding author: Edgar Maqueda (emaqueda@ing.una.py)

ABSTRACT A variable-speed predictive torque control (PTC) of a six-phase induction machine (SPIM) fed by a multi-modular matrix converter (M-MMC) is presented in this paper. This new system inherits the advantages of both multiphase machines (i.e., inherent fault-tolerance and better distribution of the power/current per phase compared to three-phase machines) and the M-MMC (i.e., smaller size and weight, and has no bulky storage elements). In addition, with the M-MMC topology, it is possible to use two power generation sources of different characteristics instead of a single three-phase source. This article proposes a method that reduces the number of calculations significantly compared to conventional PTC to overcome this issue. Simulation and experimental results are provided for speed control, module failure performance and tolerance to the variation of the magnetization inductance of the SPIM. An experimental test bench on a customized SiC-Mosfets based M-MMC and a 5.5 kW symmetrical SPIM has been used.

INDEX TERMS Multi-modular matrix converter, predictive torque control, six-phase induction machine.

I. INTRODUCTION

Multiphase electric drives are increasingly considered for the research and industry communities as a good option for generation and traction systems [1]. This system has several advantages despite its complexity compared to the traditional three-phase system, i.e., its fault-tolerant capability (with no extra hardware) and the possibility to split the power (or current) of the electrical driver into a greater number of phases and therefore reducing the converter rating per phase [2]–[4]. These points constitute the reasons for the development of multiphase electrical systems. Some emblematic companies in the industrial sector have already used multiphase systems to solve some of their product lines. The Hyundai company has an ultra-high-speed elevator based on a nine-phase permanent magnet synchronous motor. The drive system is made

The associate editor coordinating the review of this manuscript and approving it for publication was Feifei Bu[ID].

by three back-to-back (BTB) three-phase power converters connected in parallel. Another example is the wind turbine of Gamesa. The wind energy system consists of a medium speed 12-phase permanent magnet synchronous generator and uses four two-level BTB three-phase power converters all connected in parallel [5].

Power converters represent one of the key elements needed for high-performance multiphase machine applications [6]. The most common choice is the well-known BTB voltage source converter (VSC) [7]–[9]. However, new research trends point to using power converters that offer better characteristics than BTB topology in terms of size, weight, and lifespan [10], [11]. Therefore, the matrix converter (MC) emerges as a good option that provides a three-phase sinusoidal voltage with variable amplitude and frequency using fully controlled bi-directional switches (Bi-Sw). Moreover, MC does not need the use of energy storage elements (capacitors or inductors) [12], [13]. Implementing a modular scheme

of three-phase direct matrix converters, also called a multi-modular matrix converter (M-MMC), had been proposed with success in six-phase generation systems to supply three-phase loads [14], [15]. M-MMC has also been introduced to interconnect the generation stage with the grid, showing interesting advantages [16]. One of the main motivations of this work is to investigate the introduced advantages by using the M-MMC in conjunction with a multiphase (six-phase) induction machine (SPIM). In this sense, using the multi-modular topology allows to use two independent input power supplies. A practical example is a local water supply network with a six-phase SPIM motor pump, where the SPIM can be powered by a three-phase AC generator by one module and the commercial power grid by the other. The idea of this system is to provides greater assurance that the motor pump will continue operating in the case of faults in any of its power supplies.

On the other hand, predictive torque control (PTC) has been applied successfully for an actual number of applications [17], [18], including SPIM fed a two-level voltage source inverter [19], [20] and three-phase machines fed by MC [21], [22]. According to the best of the authors' knowledge, PTC has neither been proposed nor tested experimentally in the literature for this new system composed of M-MMC and a SPIM. PTC offers the same advantages of finite-set model predictive control (FS-MPC), namely, the control method is straightforward, with fast dynamic performance, and there is no need for a modulator that is useful when MC and/or multiphase machines are used. However, FS-MPC also has some drawbacks. One of them is the high computational burden needed in higher-level systems, as the one proposed in this paper.

SPIMs are peculiar devices, and, consequently, they require unconventional power electronic converters to drive them. Multiphase drives represent an issue to be solved before the use of SPIMs. This work seeks to contribute to the field of multiphase drives using the M-MMC to feed the SPIM. The main contribution of this work is the experimental evaluation of the performance of the proposed system based on a three-phase MC within a multi-modular topology to feed a SPIM. In addition, a valid vector reduction system is implemented to reduce the computational burden involved in the real-time implementation.

The rest of this paper is divided as follows. Section II presents the mathematical model of the system. The outer speed control and the proposed PTC strategy are presented in Section III. Simulations and experimental validation of the proposal in a real-time platform in transient and steady-state conditions are developed in Section IV. Obtained results under fault and parameter mismatch conditions are also presented in the same section. The last section summarizes the conclusions.

II. POWER CONVERSION SYSTEM
The proposed energy conversion system is based on the MC, which is used within the multi-modular topology to
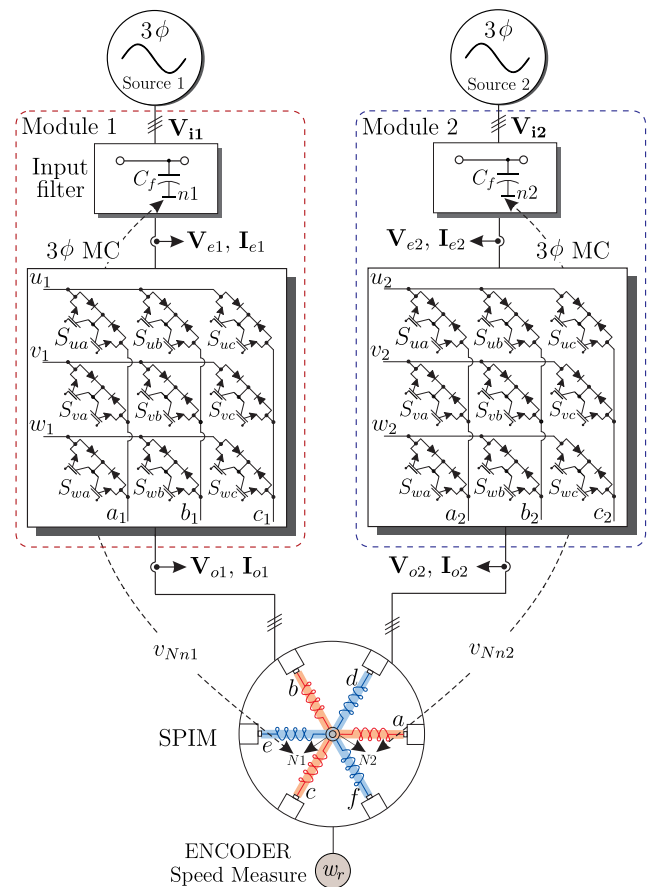

FIGURE 1. Schematic diagram of the SPIM fed by an M-MMC.

feed a symmetric SPIM as seen in Fig. 1. It is essential to highlight that two modules of three-phase MCs form the M-MMC.

A. MULTI-MODULAR MATRIX CONVERTER TOPOLOGY
The M-MMC topology consists of the integration of two three-phase MC connected to each of the converter's inputs through the intermediary of the filter (C_f) and six columns as outputs in total. Each one of these modules is represented by the power scheme of Fig. 1. In this case, the input source of the M-MMC is indicated as $\mathbf{V}_{ej} = [v_{uj}, v_{vj}, v_{wj}]^T$ and $\mathbf{I}_{ej} = [i_{uj}, i_{vj}, i_{wj}]^T$ where $j \in \{1, 2\}$ and T is the transpose matrix. The output voltages of the MC to the corresponding SPIM neutral point (N_j) is $\mathbf{V}_{oj} = [v_{oaj}, v_{obj}, v_{ocj}]^T$. Moreover, output currents are $\mathbf{I}_{oj} = [i_{oaj}, i_{obj}, i_{ocj}]^T$. Each MC is composed of nine Bi-Sw, which can generate 27 feasible switching states [23]. Then the following vectorial equations relate the input and output voltages and currents through the switching states of the MC:

$$\mathbf{V}_{onj} = \mathbf{S} \cdot \mathbf{V}_{ej}, \quad \mathbf{I}_{ej} = \mathbf{S}^T \cdot \mathbf{I}_{oj}, \quad (1)$$

where $\mathbf{V}_{onj} = [v_{oanj}, v_{obnj}, v_{ocnj}]^T$ is the MC's three-phase output voltage vector in reference to point n formed by

the input filter and $\mathbf{S}$ is the instantaneous transfer matrix, defined as:

$$\mathbf{S} = \begin{bmatrix} S_{ua} & S_{ub} & S_{uc} \\ S_{va} & S_{vb} & S_{vc} \\ S_{wa} & S_{wb} & S_{wc} \end{bmatrix}, \tag{2}$$

and the elements of the matrix $\mathbf{S} \in \{0, 1\}$ represent the state of the corresponding switch. The voltage $\mathbf{V}_{oj}$ is obtained using (3):

$$\mathbf{V}_{oj} = \mathbf{V}_{onj} - \mathbf{V}_{Nnj}, \tag{3}$$

where $\mathbf{V}_{Nnj} = [v_{Nnj}, v_{Nnj}, v_{Nnj}]^T$ is the voltage between the neutral points and $v_{Nnj} = \frac{1}{3}(v_{oanj} + v_{obnj} + v_{ocnj})$.

To avoid short circuits on the input side and ensure an uninterrupted current flow on the load side, the switching signals S_{xy} must satisfy the following condition [24]:

$$S_{uy} + S_{vy} + S_{wy} = 1. \quad y \in \{a, b, c\}. \tag{4}$$

Finally, if the six-phase vectors of output voltages and currents are defined as:

$$\mathbf{V}_o = [v_{oa1}, v_{ob1}, v_{oc1}, v_{oa2}, v_{ob2}, v_{oc2}]^T,$$
$$\mathbf{I}_o = [i_{oa1}, i_{ob1}, i_{oc1}, i_{oa2}, i_{ob2}, i_{oc2}]^T.$$

B. SPIM MODEL

The mathematical modelling of SPIM is studied extensively by various research papers, and they are presented in detail in [25]. Differential equations describe the SPIM model with time-dependent coefficients. Using the appropriate transformations of the stator and rotor phase variables, a mathematical model of a SPIM with constant coefficients is obtained [26]. The final equations of the SPIM take the form in the stationary frame of reference in which it is presented below:

$$\frac{di_{\alpha s}}{dt} = -\frac{1}{\tau_\sigma} i_{\alpha s} + \frac{k_r}{\sigma L_s \tau_r} \psi_{\alpha r} + \frac{k_r w_r}{\sigma L_s} \psi_{\beta r} + \frac{1}{\sigma L_s} v_{\alpha s}, \tag{5}$$

$$\frac{di_{\beta s}}{dt} = -\frac{1}{\tau_\sigma} i_{\beta s} + \frac{k_r}{\sigma L_s \tau_r} \psi_{\beta r} - \frac{k_r w_r}{\sigma L_s} \psi_{\alpha r} + \frac{1}{\sigma L_s} v_{\beta s}, \tag{6}$$

where R_s, R_r, L_m, $L_r = L_{lr} + L_m$ and $L_s = L_{ls} + L_m$ are the electrical parameters of the SPIM, and the constants are defined as $k_r = \frac{L_m}{L_r}$, $k_s = \frac{L_m}{L_s}$, $\sigma = 1 - \frac{L_m^2}{L_s L_r}$, $\tau_\sigma = \frac{\sigma L_s}{r_\sigma}$, $\tau_r = \frac{L_r}{R_r}$ and $r_\sigma = R_s + k_r^2 R_r$. Similarly, the dynamics of the rotor flux in the plane $\alpha - \beta$ is given by:

$$\frac{d\psi_{\alpha r}}{dt} = \frac{L_m}{\tau_r} i_{\alpha s} - \frac{1}{\tau_r} \psi_{\alpha r} - w_r \psi_{\beta r}, \tag{7}$$

$$\frac{d\psi_{\beta r}}{dt} = \frac{L_m}{\tau_r} i_{\beta s} - \frac{1}{\tau_r} \psi_{\beta r} + w_r \psi_{\alpha r}. \tag{8}$$

The stator flux is given as follows:

$$\psi_{\alpha s} = \sigma L_s i_{\alpha s} + k_r \psi_{\alpha r}, \quad \psi_{\beta s} = \sigma L_s i_{\beta s} + k_r \psi_{\beta r}, \tag{9}$$

and its derivative as:

$$\frac{d\psi_{\alpha s}}{dt} = v_{\alpha s} - R_s i_{\alpha s}, \quad \frac{d\psi_{\beta s}}{dt} = v_{\beta s} - R_s i_{\beta s}. \tag{10}$$
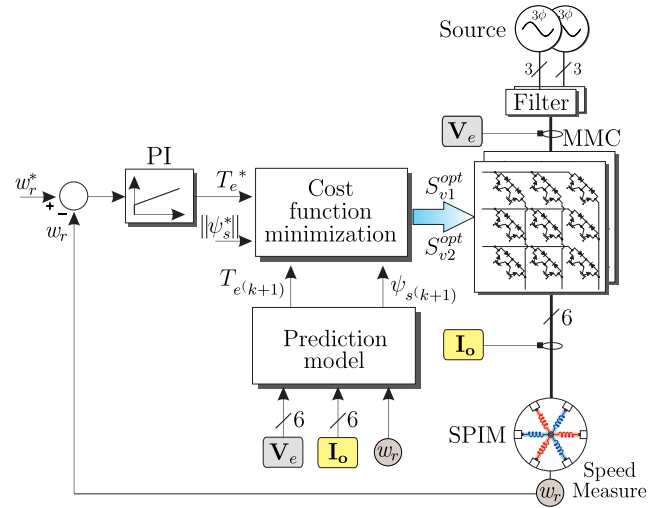

FIGURE 2. Block diagram of the control strategy.

On the other hand, the $x - y$ components (related to the SPIM's losses) only involve the stator resistance and leakage inductance:

$$v_{xs} = R_s i_{xs} + \frac{d\psi_{xs}}{dt}, \quad \psi_{xs} = L_{ls} i_{xs}, \tag{11}$$

$$v_{ys} = R_s i_{ys} + \frac{d\psi_{ys}}{dt}, \quad \psi_{ys} = L_{ls} i_{ys}. \tag{12}$$

The modelling of the SPIM in its decomposition of the vector space in its six-phase dimensions input defined by (a, b, c, d, e, f), where the model is represented in three different orthogonal planes called two-dimensional stationary reference planes $\alpha - \beta$, $x - y$ and $z_1 - z_2$ using (13), where the invariant amplitude criteria has been considered [27].

$$\mathbf{T} = \frac{1}{3} \begin{bmatrix} 1 & -\frac{1}{2} & -\frac{1}{2} & \frac{1}{2} & \frac{1}{2} & -1 \\ 0 & -\frac{\sqrt{3}}{2} & \frac{\sqrt{3}}{2} & \frac{\sqrt{3}}{2} & -\frac{\sqrt{3}}{2} & 0 \\ 1 & -\frac{1}{2} & -\frac{1}{2} & -\frac{1}{2} & -\frac{1}{2} & 1 \\ 0 & \frac{\sqrt{3}}{2} & -\frac{\sqrt{3}}{2} & \frac{\sqrt{3}}{2} & -\frac{\sqrt{3}}{2} & 0 \\ 1 & 1 & 1 & 0 & 0 & 0 \\ 0 & 0 & 0 & 1 & 1 & 1 \end{bmatrix}. \tag{13}$$

The SPIM is symmetrical, so it has a phase shift of 60° between the three phases and has an isolated neutral configuration. Thus $z_1 - z_2$ currents are considered null. Using (5) through (12) it is possible to obtain a mathematical model that represents the dynamics of the expressed system in the stationary frame of reference as follows:

$$\dot{\mathbf{X}}_{(t)} = \mathbf{A}_{(t)} \cdot \mathbf{X}_{(t)} + \mathbf{B}_{(t)} \cdot \mathbf{U}_{(t)}, \tag{14}$$

$$\mathbf{F}_{(t)} = \mathbf{C}_{(t)} \cdot \mathbf{G}_{(t)}, \tag{15}$$

where $\mathbf{X}_{(t)} = [x_1, x_2, x_3, x_4, x_5, x_6]^T$ is the state vector which represents the stator currents and flux $x_1 = i_{\alpha s}$,

$x_2 = i_{\beta s}$, $x_3 = i_{xs}$, $x_4 = i_{ys}$, $x_5 = \psi_{\alpha r}$ and $x_6 = \psi_{\beta r}$, $\mathbf{U}_{(t)} = \begin{bmatrix} v_{\alpha s}, & v_{\beta s}, & v_{xs}, & v_{ys} \end{bmatrix}^T$ is the input voltage vector applied to the stator and rotor windings, $\mathbf{F}_{(t)} = \begin{bmatrix} \psi_{\alpha s}, & \psi_{\beta s}, & \psi_{xs}, & \psi_{ys} \end{bmatrix}^T$ is the stator flux, where $\mathbf{G}_{(t)} = \begin{bmatrix} i_{\alpha s}, & i_{\beta s}, & i_{xs}, & i_{ys}, & \psi_{\alpha r}, & \psi_{\beta r} \end{bmatrix}^T$, all written in $\alpha - \beta$ and $x - y$ frame. $\mathbf{A}_{(t)}$, $\mathbf{B}_{(t)}$ and $\mathbf{C}_{(t)}$ are matrices defined by the electrical parameters of the SPIM where the coefficient $c_1 = \sigma L_s$ and $c_2 = L_{ls}$, w_r is rotor speed, as follows:

$$\mathbf{A}_{(t)} = \begin{bmatrix} -\dfrac{1}{\tau\sigma} & 0 & 0 & 0 & \dfrac{k_r}{c_1\tau_r} & \dfrac{k_r w_r}{c_1} \\ 0 & -\dfrac{1}{\tau\sigma} & 0 & 0 & -\dfrac{k_r w_r}{c_1} & \dfrac{k_r}{c_1\tau_r} \\ 0 & 0 & -\dfrac{R_s}{c_2} & 0 & 0 & 0 \\ 0 & 0 & 0 & -\dfrac{R_s}{c_2} & 0 & 0 \\ \dfrac{L_m}{\tau_r} & 0 & 0 & 0 & -\dfrac{1}{\tau_r} & -w_r \\ 0 & \dfrac{1}{\tau_r} & 0 & 0 & w_r & -\dfrac{1}{\tau_r} \end{bmatrix},$$

$$\mathbf{B}_{(t)} = \begin{bmatrix} \dfrac{1}{c_1} & 0 & 0 & 0 \\ 0 & \dfrac{1}{c_1} & 0 & 0 \\ 0 & 0 & \dfrac{1}{c2} & 0 \\ 0 & 0 & 0 & \dfrac{1}{c2} \end{bmatrix},$$

$$\mathbf{C}_{(t)} = \begin{bmatrix} c_1 & 0 & 0 & 0 & k_r & 0 \\ 0 & c_1 & 0 & 0 & 0 & k_r \\ 0 & 0 & c_2 & 0 & 0 & 0 \\ 0 & 0 & 0 & c_2 & 0 & 0 \end{bmatrix}.$$

Finally, the electromagnetic torque (T_e) of the SPIM is expressed as follows:

$$T_e = 3P(\psi_{\alpha s}i_{\beta s} - \psi_{\beta s}i_{\alpha s}), \tag{16}$$

being P the pole pair number of the SPIM.

III. PROPOSED CONTROL STRATEGY

The PTC has the same advantages as FC-MPC strategy, such as being easy to understand, easy to implement, can deal with nonlinearities, and can handle several variables simultaneously [28]. PTC has some similarities and differences compared to the two main control strategies for electrical drives: Field-Oriented Control (FOC) and Direct Torque Control (DTC). The three control strategies (FOC, DTC and PTC) need a speed PI control for realizing the adjustable speed control for a SPIM. FOC uses four current PI controllers for the inner controllers; DTC uses four hysteresis controllers and a Lookup Table (LUT), and PTC takes a cost function to evaluate the torque and flux magnitude errors. FOC needs coordinate transformation, and therefore, flux angle is necessary. DTC and PTC algorithms are in the stator reference frame, so no coordinate transformation is required; however, for the use of LUT, DTC needs the calculation of stator flux

angle, though the angle serves for sector selection and its precision of estimation is not that crucial as MPCs. FOC needs a modulator to handle the continuous variables, and the other two methods make the modulator absent due to their direct control features. As for the tuning works, FOC has five PI controllers, in which ten parameters need to be calculated and tuned. DTC requires six parameters, among which two are for PI controllers, and the other four are for hysteresis system. PTC needs three parameters with two for PI controllers and one weighting factor for cost function [29].

Then, the proposed control strategy consists of a PI controller in conjunction with the PTC. An external PI controller performs the speed control. This controller receives the measured rotational speed from the SPIM and generates the appropriate machine torque reference as a function of the desired speed. The inner PTC loop inner loop uses this torque reference and the stator electromagnetic flux reference. The latter searches for the best M-MMC switching state to generate the appropriate output voltage to be applied to the SPIM and thus achieve torque and flux levels similar to the reference. Fig. 2 exhibits the control scheme.

A. PI SPEED CONTROL

The mechanical speed control of the SPIM is performed indirectly by the PI controller, which generates a torque response at the output in relation to the desired and measured speed of the SPIM. This torque response at the controller output represents the necessary reference for the PTC strategy. The PI controller designed to control the plant is based on the mechanical model of the SPIM, considering that the load torque is a disturbance to the system, which is defined by the following transfer function:

$$\frac{w_r(s)}{T_e(s)} = \frac{1}{sJ}, \tag{17}$$

where J is the moment inertia of the SPIM, respectively. The approximate bandwidth is 10 Hz, and it is considered that data for the controller design.

B. INNER PTC STRATEGY

The FS-MPC technique finds which switching vector should be applied in the next sampling period from among a set of possible vectors through predictive calculations of the system variables' behaviour in a given horizon. Therefore, for the PTC, first, the mathematical model describing the system's dynamics to be controlled must be obtained. Then, the best voltage vector that meets the desired value must be sought, using a minimization technique. Thus, the SPIM prediction model must be designed to obtain the desired electromagnetic torque T_e^* to apply PTC to SPIM. The prediction of the rotor flux is also required to control the machine. In this case, the discrete version is used applying the Euler discretization method in (7) and (8).

$$\psi_{r\alpha}(k+1) = \frac{L_m T_s}{\tau_r}i_{\alpha s} + \left(1 - \frac{T_s}{\tau_r}\right)\psi_{\alpha r}(k) - w_r T_s \psi_{\beta r}(k), \tag{18}$$

$$\psi_{r\beta}(k+1) = \frac{L_m T_s}{\tau_r} i_{\beta s} + \left(1 - \frac{T_s}{\tau_r}\right) \psi_{\beta r}(k)$$
$$- w_r T_s \psi_{\alpha r}(k), \tag{19}$$

where T_s is the sampling time and $v_{\alpha s}$, $v_{\beta s}$, $i_{\alpha s}$, $i_{\beta s}$, the MC output voltages and currents calculated by (1) for each phase and then transformed by (20) to the $\alpha - \beta$ plane.

$$\mathbf{V_s}[\alpha\beta] = \mathbf{T} \cdot \mathbf{V_o} \quad \mathbf{I_s}[\alpha\beta] = \mathbf{T} \cdot \mathbf{I_o}. \tag{20}$$

The prediction of stator currents is obtained from (5) and (6), resulting in:

$$i_{s\alpha}(k+1) = \left(1 - \frac{T_s}{\tau_r}\right) i_{s\alpha}(k) + \frac{k_r T_s}{\sigma L_s \tau_r} \psi_{r\alpha}(k)$$
$$+ \frac{k_r w_r T_s}{\sigma L_s} \psi_{r\beta}(k) + \frac{T_s}{\sigma L_s} v_{s\alpha}(k), \tag{21}$$

$$i_{s\beta}(k+1) = \left(1 - \frac{T_s}{\tau_r}\right) i_{s\beta}(k) + \frac{k_r T_s}{\sigma L_s \tau_r} \psi_{r\beta}(k)$$
$$- \frac{k_r w_r T_s}{\sigma L_s} \psi_{r\alpha}(k) + \frac{T_s}{\sigma L_s} v_{s\beta}(k), \tag{22}$$

then, from (9) the prediction of the stator fluxes is obtained as follows:

$$\psi_{s\alpha}(k+1) = \sigma L_s i_{s\alpha}(k+1) + k_r \psi_{r\alpha}(k+1), \tag{23}$$
$$\psi_{s\beta}(k+1) = \sigma L_s i_{s\beta}(k+1) + k_r \psi_{r\beta}(k+1). \tag{24}$$

The prediction of the T_e is obtained as:

$$T_e(k+1) = 3P(\psi_{s\alpha}(k+1)i_{s\beta}(k+1)$$
$$- \psi_{s\beta}(k+1)i_{s\alpha}(k+1)). \tag{25}$$

Then, the predicted errors for each of the possible switching vectors are determined. This error generated by each vector is evaluated through an equation called cost function (g). It is possible to incorporate within g the search for different targets within the FS-MPC algorithm using appropriate weight factors for each target. In this case, g is defined as a quadratic measure of the predicted error and is represented as follows:

$$g = |T_e^* - T_e(k+1)| + \lambda_\psi |\psi_s^* - \psi_s(k+1)|, \tag{26}$$

where ψ_s^* and $\psi_s(k+1)$ are the reference and predicted stator flux, respectively. The λ_ψ is weighting factor for stator flux and it is calculated as the ratio of the nominal torque of the machine and the reference flux $\lambda_\psi = \frac{T_e}{\psi_s^*}$. Finally, after the evaluation of all possible vectors, the algorithm selects the optimal switching vector that meets the value desired by the prediction objective, which will be applied in the next sampling period.

C. SPACE VECTORS AND SWITCHING STATE REDUCTION

Each three-phase MC has 27 valid switching states (S_v), and the M-MMC also has 27×27 equivalent to $S_v = 729$ valid switching states. This number of M-MMC's states represents a significant problem for real-time implementation due to the number of calculations. MPC requires a larger amount of computation compared to classical controllers [28], [29].
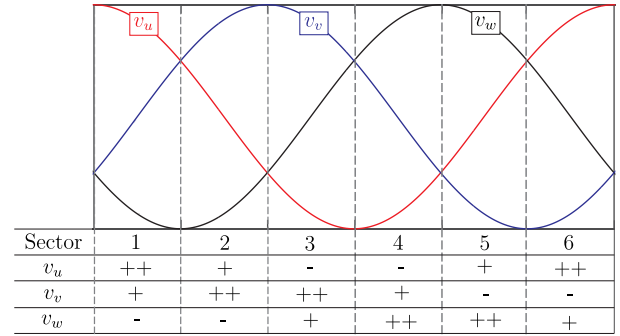
FIGURE 3. Input source sectorization.

Sector	1	2	3	4	5	6
v_u	++	+	-	-	+	++
v_v	+	++	++	+	-	-
v_w	-	-	+	++	++	+

TABLE 1. Selection of switching states of each three-phase module of the M-MMC.

Sector	Selected switching states
1	1, 2, 3, 4, 5, 6, 7, 10, 13, 16, 19, 22, 25
2	1, 2, 3, 4, 5, 6, 8, 11, 14, 17, 20, 23, 25
3	1, 2, 3, 4, 5, 6, 9, 12, 15, 18, 21, 24, 25

This fact leads to an increase in the computational time of the control algorithm. The reduction of vectors in the M-MMC makes it possible to reduce the amount of computations of the MPC control algorithm, thus benefiting its experimental implementation. A minimal computational time also gives the benefit of reducing the passive elements of the MC input filters. Each of the 27 valid states of the MC, depending on the input phases, generates at the output different voltages expressed in spatial vectors [30]. Fig. 3 shows the division into sectors of the phases of the input voltage to a three-phase MC. Each sector in Fig. 3 considers the difference in voltage levels of the input voltage that is repeated in each period. The $++, +$ and $-$ symbols represent the highest, middle and lowest amplitude of all, respectively.

On the other hand, Fig. 4(a) and Fig. 4(b) show the distribution of the space vectors in the $\alpha - \beta$ plane for sectors 1 and 4 of the Fig. 3. Both Fig. 4(a) and Fig. 4(b) practically represent the same shape, with the difference in the number of space vectors generated, which is due to the order and levels of the MC input voltage. In this work, a strategy was proposed to use the space vectors with the largest amplitude and only one zero vector to reduce the number of M-MMC vectors, with which the highest voltages can be reached at the output of the MC and cross practically the whole area of the space vector. Sectors 1 and 4, 2 and 5, 3 and 6 generate the same number of space vectors at the output. Therefore, the latter sectors are reduced to three. Table 1 shows the switching vectors used by each sector. Finally, the results show 13 selected states of the MC and $S_v = 169$ valid vectors in the M-MMC. This strategy contemplates performing one iteration of $S_v = 169$ vectors for each input sector. Fig. 4(c) shows the space vectors in the $\alpha - \beta$ plane formed by each of the 169 resulting M-MMC vectors corresponding to an input voltage for sector 1 for both modules.
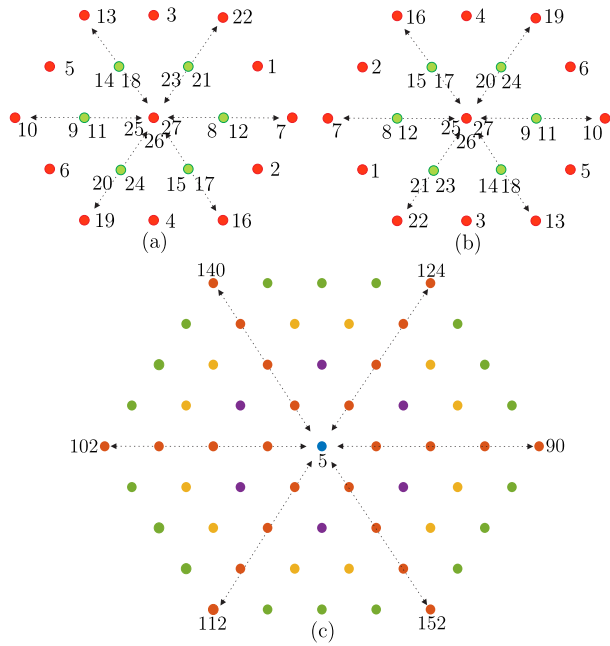
FIGURE 4. Output voltage spatial vectors in the plane $\alpha - \beta$.
(a) Three-phase MC of input source sector 1. (b) Three-phase MC of input source sector 4 and (c) Six-phase M-MMC of input source sector 1.

D. ALGORITHM DESCRIPTION

Algorithm 1 describes the steps of the PTC with $S_v = 129$ used in both the simulation and the experimental platform. The measured variables are the input phase voltages $\mathbf{V}_{e1}$, $\mathbf{V}_{e2}$ and the output currents $\mathbf{I}_o$, as shown in step 1. The currents are transformed to the $\alpha - \beta$ plane in step 3, while the rotor flux is estimated in step 4. For each of the three sectors of Table 1, the output voltages of each MC are calculated, for each of the 13 valid vectors, using the cycles **for$_1$** and **for$_2$**, step 5 to 8. Next, the output voltages of each MC are calculated with reference to the N_j point of the machine $\mathbf{V}_{o1}$ and $\mathbf{V}_{o2}$, the rotor flux, the stator current, and flux, and the electromagnetic torque are predicted. Finally, the cost function g_{opt} is minimized, the optimal vector S_{v1}^{opt} and S_{v2}^{opt} are selected, and the following sampling time is applied, steps 9 to 22, respectively.

IV. RESULTS

The results are presented in two groups: i) an evaluation in the simulation environment of the SPIM speed control powered by the M-MMC using an internal PTC and, ii) experimental results based on a M-MMC designed with SiC-MOSFETs and a 5.5 kW SPIM. In addition, the behavior of the proposed system to faults of one of the M-MMC modules and the tolerance to discrepancies in the L_m of the SPIM are presented.

A. SIMULATION RESULTS

The results in this section consist of an evaluation in the Matlab Simulink environment. The evaluation of the SPIM PTC fed by the M-MMC is presented. A reference velocity and electromagnetic flux are established to verify the

---

Algorithm 1 Algorithm Implemented in the Control Platform

1. Read measured $\mathbf{V}_{e1}$, $\mathbf{V}_{e2}$, $\mathbf{I}_o$ and w_r
2. Initialize $g_{opt} := \infty$, $\psi_s^{opt} := 0$
3. Calculate stator currents $\mathbf{I}_s[\alpha\beta]$ using (20)
4. Rotor flux is estimated using (18) and (19)
5. **if $\mathbf{V}_e ==$ Sector$_i$ then** $i \in \{1, 2, 3\}$
6.   **for$_1$** $j_1 = 1$ **to** 13
7.   Calculate the output voltage $\mathbf{V}_{o1}$ using (3)
8.   **for$_2$** $j_2 = 1$ **to** 13
9.   Calculate the output voltage $\mathbf{V}_{o2}$ using (3)
10.   Calculate six-phase output voltage $\mathbf{V}_s[\alpha\beta]$ using (20)
11.   Predict the rotor flux in $(k + 1)$ using (18) and (19)
12.   Predict the stator current in $(k + 1)$ using (21) and (22)
13.   Predict the stator flux in $(k + 1)$ using (23) and (24)
14.   Calculate the electromagnetic torque using (25)
15.   Minimize cost function g using (26)
16.   **if** $g < g_{opt}$ **then** (Select optimal vector)
17. $g_{opt} \leftarrow g, S_{v1}^{opt} \leftarrow S_v(j_1), S_{v2}^{opt} \leftarrow S_v(j_2)$,
18. $\psi_s^{opt} \leftarrow \psi_s$, **end if**
19.   **end for$_2$**
20.   **end for$_1$**
21. **end if**
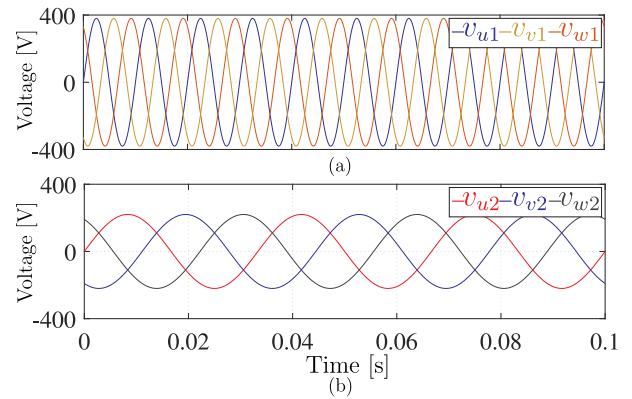22. Apply the optimum vector $S_v^{opt} \in \{S_{v1}^{opt}, S_{v2}^{opt}\}$

FIGURE 5. Three-phase power supply of the M-MMC. (a) Source 1 = 380 V, 100 Hz and (b) Source 2 = 220 V, 30 Hz.

behaviour of the proposed system for changes in velocity and mechanical load. Results were obtained at sampling frequencies of $f_s = 10$ kHz and $f_s = 100$ kHz. In addition, the system is tested with different input sources for each module, and the waveforms of the supply current and the output current of the M-MMC are verified. The used parameters for the simulation are presented in Table 2.

By means of the M-MMC topology it is possible to use two three-phase power generation sources of different characteristics, in terms of amplitude and frequency. In this context, for the simulation tests, the input power supplies were used as shown in Fig. 5, with values equal to 380 V, 100 Hz and 220 V,
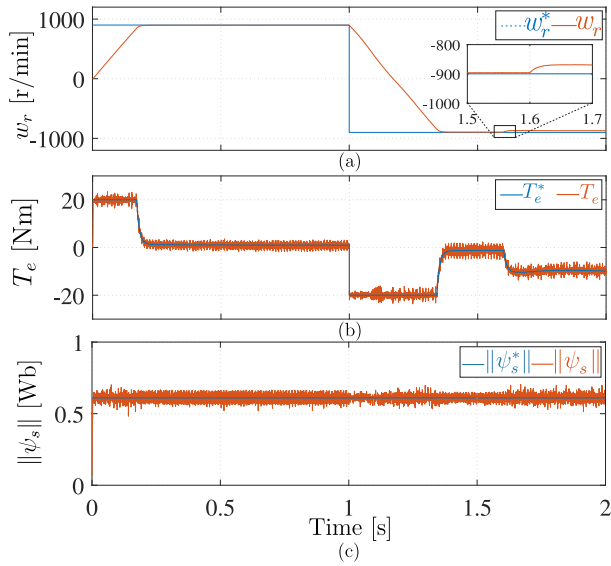
FIGURE 6. Simulation results of behavior at $f_s = 10$ kHz of (a) mechanical speed, (b) electrical torque and (c) magnitude of stator flux while the speed reference is changing from 900 r/min to -900 r/min.
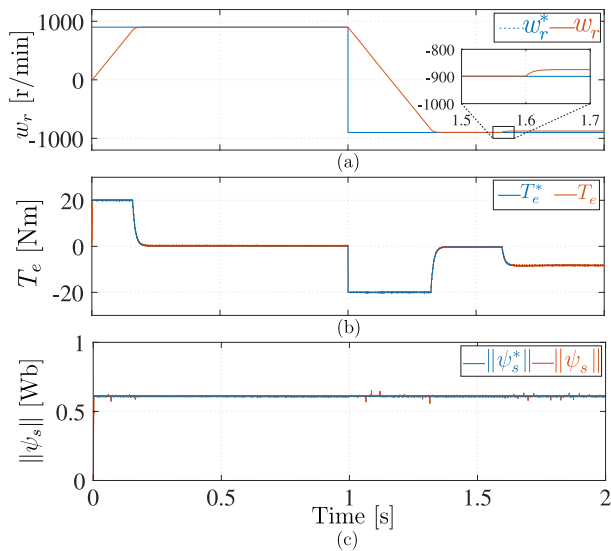

FIGURE 7. Simulation results of behavior at $f_s = 100$ kHz of (a) mechanical speed, (b) electrical torque and (c) magnitude of stator flux while the speed reference is changing from 900 r/min to -900 r/min.
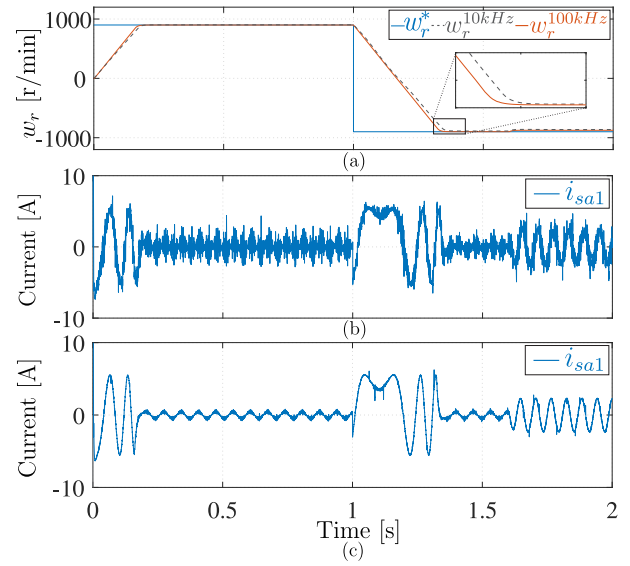

FIGURE 8. Waveform of the M-MMC output current applied to the SPIM, (a) mechanical velocity follow up, (b) output current with $f_s = 10$ kHz. and (c) output current with $f_s = 100$ kHz.
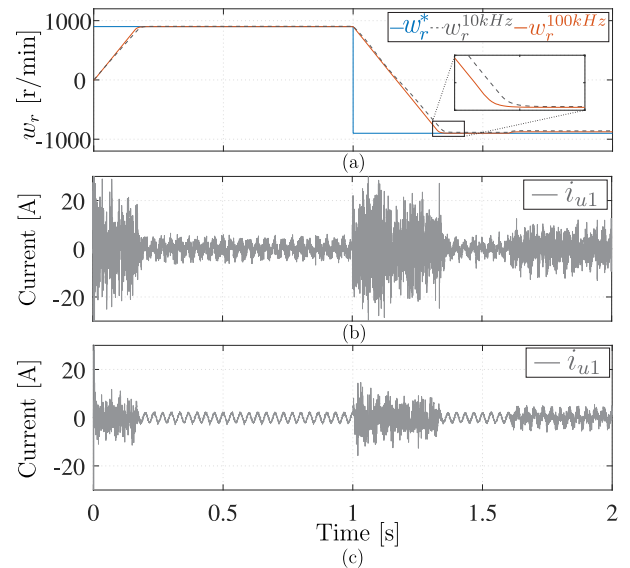

FIGURE 9. Waveform of the M-MMC supply current applied to the SPIM, (a) mechanical velocity follow up, (b) input current with $f_s = 10$ kHz. and (c) input current with $f_s = 100$ kHz.

30 Hz for sources 1 and 2, respectively. The results in velocity, torque and electromagnetic flux tracking of the SPIM fed by the M-MMC can be seen in Fig. 6 and Fig. 7 for a $f_s = 10$ kHz and $f_s = 100$ kHz, respectively. An initial speed reference of 900 r/min is set with a mechanical torque of 0.2 Nm. Next, a speed change to -900 r/min is performed and finally a load torque of 10 Nm is set in order to observe its effects mainly on the speed track.

The waveforms of the phase output current at i_{oa1} of the M-MMC are presented in Fig. 8(b) and Fig. 8(c), and for the input current supply i_{u1} in Fig. 9(b) and Fig. 9(c), for $f_s = 10$ kHz and $f_s = 100$ kHz, respectively. It is possible

to note the considerable reduction in the ripple level of the current for $f_s = 100$ kHz. This is due to the fact that as the sampling frequency in the MPC increases, the time in which the predicted vectors are updated decreases, so the error or distance between the reference vector and the predicted vector also decreases. The six waveforms of the M-MMC output current $\mathbf{I}_o$ are presented for both module 1 in Fig. 10(b) and for module 2, Fig.10(c).

B. EXPERIMENTAL RESULTS

The SPIM was designed from a commercial three-phase 5.5 kW machine, which the rewinding procedure is detailed in [31]. The proposed PTC technique was experimentally
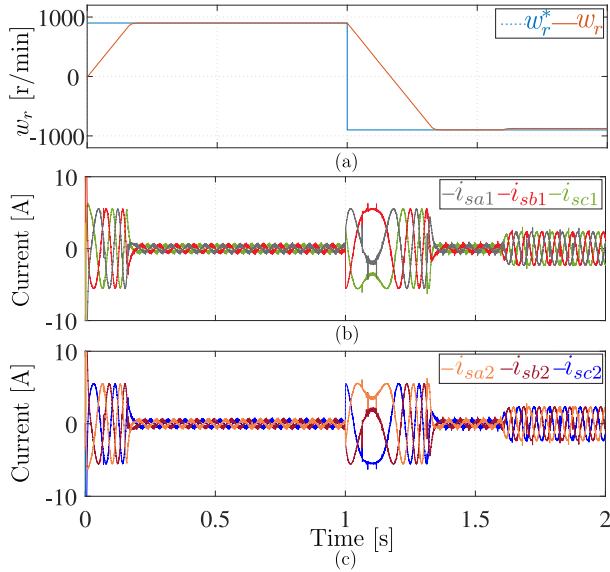
FIGURE 10. Waveform of the output currents of the six phases of the M-MMC at f_S = 10 kHz. (a) Module 1 and (b) module 2.

TABLE 2. Parameter of simulations and experimental setup.

Parameter	Description	Value
v_{u1}	Input voltage Source 1	380 V
f_{s1}	Input frequency Source 1	100 Hz
v_{u2}	Input voltage Source 2	220 V
f_{s2}	Input frequency Source 2	30 Hz
C_f	Input filter capacitor	30 μF
P_n	Nominal power of the machine	5.5 kW
w_n	Nominal speed	1430 r/min
T_n	Nominal torque	20 Nm
R_s	Stator resistance	5.95 Ω
L_{ls}	Stator inductance	7.7 mH
R_r	Rotor resistance	3.95 Ω
L_{lr}	Rotor inductance	5.1 mH
L_m	Magnetizing inductance	430 mH
P	Pair of poles	2
J	Moment of inertia	0.07 kgm^2
$\|\psi_s^*\|$	Reference flux	0.61 Wb
T_{sw}	Sampling time of the PI controller	0.0002 s
K_p	Proportional gain	3.0
K_i	Integrative gain	0.141
λ_T	Torque weighting factor	1 (Nm)$^{-1}$
λ_ψ	Flux weighting factor	50 (Wb)$^{-1}$

tested on a 10 kW M-MMC. The relevant parameters of the test bench are presented in Table 2.

The M-MMC prototype is based on Bi-Sw formed by discrete semiconductors SiC-MOSFETs (SCH2080KE). Fig. 11
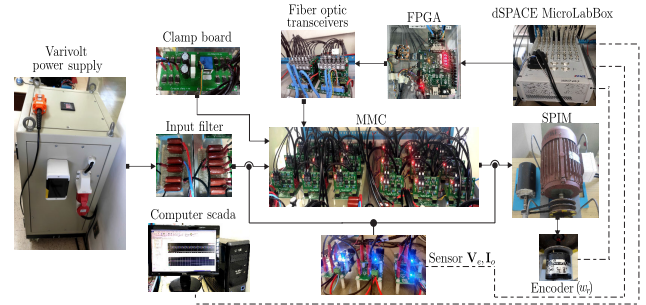

FIGURE 11. Block diagram of the test bench that includes in the central part the power supply connected to the input filter, the M-MMC and finally the SPIM. In the upper part, the dSPACE platform, and the FPGA, fiber optic and clamp circuit boards, respectively, and in the lower part the encoder, the current and voltage sensor boards and the computer.
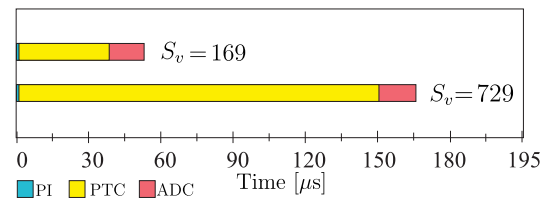

FIGURE 12. Comparison of the computational load of the PTC with the vectors S_v = 729 and S_v = 169 using the MicroLabBox dSPACE device.

presents the three-phase MC, which is created by 9 Bi-Sw and 18 SiC-MOSFETs, designed in a modular way with their respective clamp circuits for protection against over-voltages. The voltage and current sensor boards have been implemented employing LEM transducers. The digital control device is the MicroLabBox dSPACE. Then, the magnitudes of the sensed signals are received, the control algorithm is executed, and the vectors to be implemented are obtained for the next sampling time. In turn, the NEXYS 3 FPGA is used for a safe switching algorithm for the Bi-Sw. The signals are transmitted to the Bi-Sw through optical fiber cables. The SPIM is a 5.5 kW symmetrical machine connected to a dc motor through its shaft that acts as a mechanical load for the SPIM and the encoder to measure the SPIM rotational speed.

The control algorithm that uses the S_v = 769 vectors has provided a computational time of 157 μs, at the time of its implementation, which represents a very long time, in reference to the sampling times used for the converter control systems in the literature, generally a minimum sampling time of 100 μs is used [32]. For this reason, this strategy has not been able to obtain experimental results. The experimental results of the proposed system have been obtained using the control strategy S_v = 169 proposed in this work. In Fig. 12, a comparison between the computational loads of running the PI, the PTC, and the ADCs is presented, where the PTC represents the highest computational load as well as the factor where strategies can be applied to optimize the computational load. With S_v = 169, the control algorithm takes a computational time of 42 μs and reduces the computational burden in approximately 74% with respect to
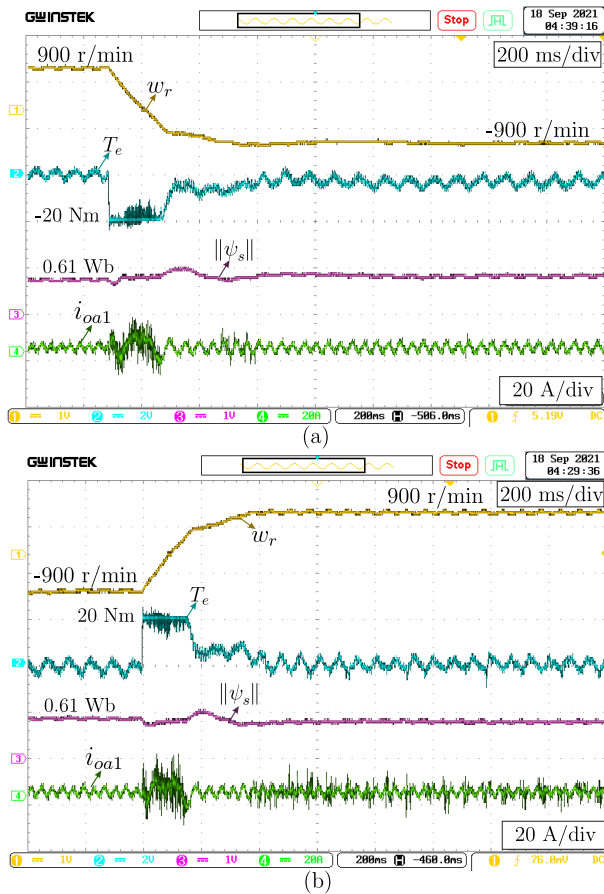
FIGURE 13. Experimental results of SPIM speed control using the M-MMC. Torque follow-up, stator flux magnitude and output current waveform i_{oa1}. (a) Mechanical speed follow-up for a change in the reference from 900 r/min to -900 r/min, (b) mechanical speed follow-up for a change in the reference from -900 r/min to 900 r/min.
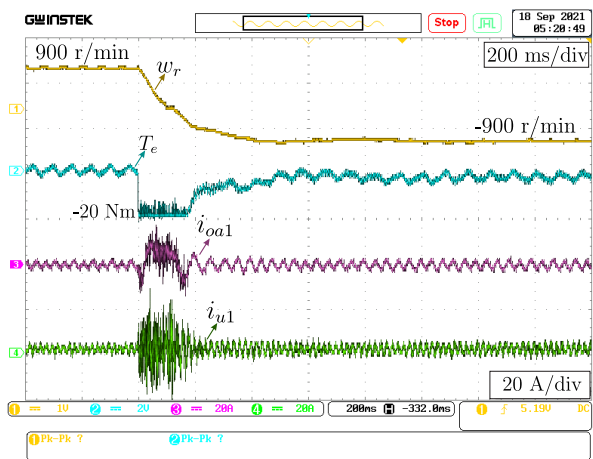

FIGURE 14. Experimental results of the speed and torque control of the SPIM fed by the M-MMC. Waveforms of the output current i_{oa1} and the supply current i_{u1} of the M-MMC.

$S_v = 729$ vectors. The sampling time $(T_s) = 50\ \mu$s was used to obtain the experimental results of the prototype.

The speed and flux references set for the experiment were 900 r/min and 0.61 Wb, respectively. The response of the
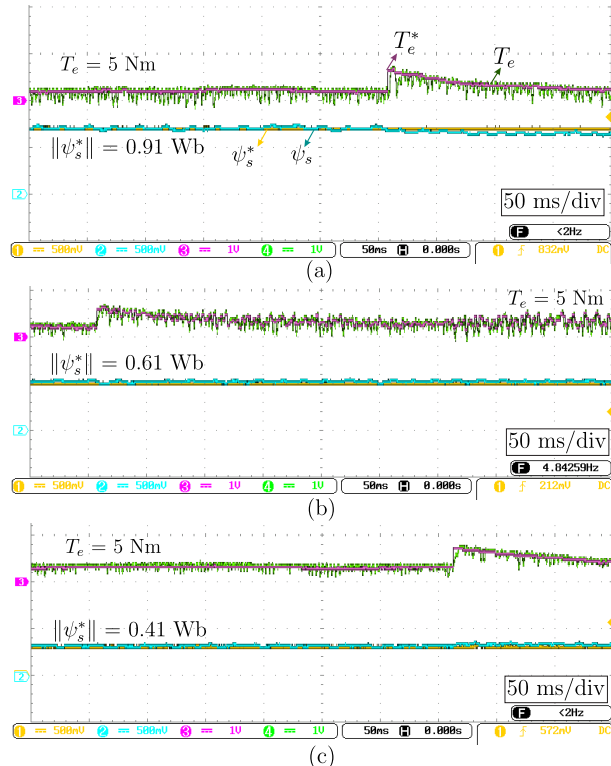

FIGURE 15. Experimental results of the SPIM control under mechanical torque variations of 0.2 Nm and 5 Nm for (a) $\|\psi_s^*\| = 0.91$ Wb, (b) $\|\psi_s^*\| = 0.61$ Wb and (c) $\|\psi_s^*\| = 0.41$ Wb.

proposed system for a change of the reference speed can be observed in Fig. 13. On the other hand, Fig. 13(a) shows the tracking of the proposed torque and electromagnetic flux control strategy and also the output current waveform i_{oa1} of the M-MMC for a speed change of 900 r/min to -900 r/min. Then, Fig. 13(b) shows the response of the system for the reverse process described above for a speed change from -900 r/min to 900 r/min. The behavior of the supply current i_{u1} and the output current i_{oa1} of module 1 were verified using Fig. 14. For the experiment, a speed change at 900 r/min was imposed and the behavior of the torque generated by the SPIM was verified. An evaluation of the proposed system against variations of mechanical torque and reference electromagnetic flux values is shown in Fig. 15. The mechanical torque change was from 0.2 Nm to 5 Nm and the reference fluxes set are 0.91 Wb, 0.61 Wb and 0.41 Wb, Fig. 15(a), Fig. 15(b) and Fig. 15(c), respectively. For this experiment, a constant reference speed equal to 300 r/min was set.

Then, a test for the fault in one of the M-MMC modules has been performed experimentally. The M-MMC and the SPIM feeder are subjected to a fault in one of its modules. In Fig. 16(a) a fault is observed in the three output phases of module 2. The waveforms of the current i_{oa1} and i_{oa2}, of modules 1 and 2, respectively, are observed for a constant speed reference of 300 r/min. In Fig. 16(b) the fault of the three phases of module 1 is presented.

In Fig. 17, a comparative analysis between MSE of torque and electromagnetic flux relative to an imposed reference
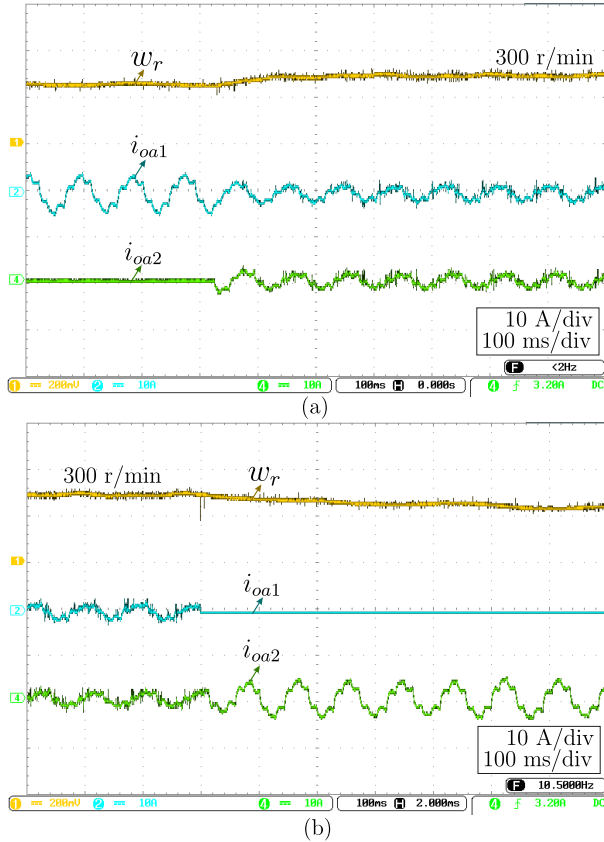
FIGURE 16. Post-fault results. Waveforms of M-MMC output current and mechanical velocity. (a) Three-phase fault of SPIM module 2 and, (b) three-phase fault of module 1.

track for different SPIM speeds is presented, the average errors 0.35 Nm and 120 μWb in torque and flux, respectively for speeds between 200 r/min and 500 r/min. A variance analysis of one of the most critical parameters of the SPIM was performed. A 25 % error of the L_m around its nominal value was considered. Table 3 shows the MSE results of the control strategy for the speed, torque and electromagnetic flux values.

C. DISCUSSION OF RESULTS

By testing in the simulation environment with different power supplies to the M-MMC, as shown in Fig. 5, it was possible to effectively validate the usefulness of the M-MMC arranged in three-phase modules taking advantage of sources of different characteristics. The results obtained in the simulation and the experimental parts can be compared and analyzed for the case of $f_s = 10$ kHz. Fig. 6, Fig. 8 and Fig. 9 can be compared with Fig. 13 and Fig. 14 which are obtained experimentally. The tracking responses of the reference speed, torque and electromagnetic flux are observed with similar characteristics. Fig. 6(a) and Fig. 7(a) show that at 1.7 s a change of the mechanical torque from 0.2 Nm to 10 Nm is realized. This effect causes an error in the velocity

TABLE 3. MSE of the control parameters at the L_m discrepancy of the SPIM.

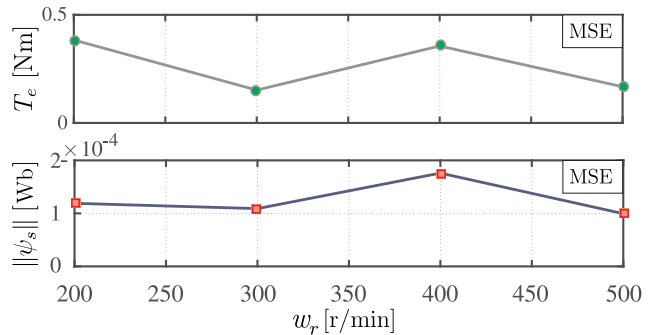| Parameter	L_m - 25 %	L_m = 430 mH	L_m + 25 %
w_n	24.34 (r/min)	21.85 (r/min)	22.63 (r/min)
T_e	0.75 (Nm)	0.31 (Nm)	0.58 (Nm)
$\|\psi_s\|$	27 (mWb)	8.7 (mWb)	16.9 (mWb)

FIGURE 17. Experimental MSE of torque and flux in reference to changes in SPIM speed.

follow-up. Using the MSE figure of merit for the velocity at that instant are 28.24 r/min and 24.38 r/min for $f_s = 10$ kHz and $f_s = 100$ kHz, respectively. The experimental results in the torque and flux tracking in the steady-state are somewhat oscillating, which is related to an imperfection of the mechanical load of the experiment, which presents small variations in the moment of rotation. The waveforms of the output current and supply current of the M-MMC can be observed very noisy in Fig. 13 and Fig. 14. However, a way to minimize this problem has been presented using a sampling frequency of the algorithm at $f_s = 100$ kHz, shown in Fig. 7, Fig. 8(c) and Fig. 9(c). We can observe a considerable reduction in the control variables ripple such as torque, flux, and thus also in the M-MMC's output and supply currents. Experimental results with $f_s = 100$ kHz were not obtained due to the high computational time required. On the other hand, it is possible to observe that in Fig. 13 and Fig. 14, there is a difference in the distortion of the stator current i_{oa1}. This phenomenon is mainly since the switching vectors applied by the M-MMC are different for both speed change situations. Consequently, the M-MMC uses a different sequence of switching vectors for a speed of 900 r/min than that of -900 r/min. The evaluations in Fig. 15 show the good tracking of the control strategy at different values set for the SPIM reference flux. Furthermore, it was possible to verify the tracking responses for a change of the mechanical torque from 0.2 Nm to 5 Nm, as shown in Fig. 15(a), Fig. 15(b) and Fig. 15(c), respectively. Experiments performed under fault conditions of one of the M-MMCs modules show that the SPIM can continue to operate with only one of the modules in operation. The increase in the output current of module 1 is observed at the time of module 2 failure in Fig. 16(a), and reciprocally in Fig. 16(b). The consequences of the fault are reflected in the variations of

the speed tracking. Consequently, the power delivered to the SPIM by the M-MMC is lost. However, note that the SPIM operates with the same control strategy under fault in one of the modules. Last, Table 3 shows the results obtaining by using a 25 % decrease of the nominal value of the L_m. The MSE of the velocity, torque, and flux is higher compared to a 25 % increase in the nominal value of the L_m. However, the results do not differ much from the nominal value, showing that the system has a robust behaviour.

V. CONCLUSION

It has been successfully demonstrated that it is possible to use the multi-modular matrix converter topology to feed a six-phase induction machine, using a speed control algorithm based on predictive torque and electromagnetic flux control. The benefits of the multi-modular topology have been demonstrated consisting of using two power supplies with different characteristics and its response to the fault of one of its modules. Moreover, a strategy to reduce the number of valid MC vectors that allow the control algorithm's implementation was also introduced. Consequently, a reduction from 729 to 169 vectors was achieved, which significantly reduced the computational time of execution of the algorithm, through which the implementation of the proposed control strategy could be achieved with a sampling time equal to 10 kHz. The results of the method demonstrate fast torque response and good follow-up of the imposed speed and electromagnetic flux as input references to the system.

REFERENCES

[1] E. Levi, "Advances in converter control and innovative exploitation of additional degrees of freedom for multiphase machines," *IEEE Trans. Ind. Electron.*, vol. 63, no. 1, pp. 433–448, Jan. 2016.

[2] M. Ayala, J. Doval-Gandoy, J. Rodas, O. Gonzalez, R. Gregor, and M. Rivera, "A novel modulated model predictive control applied to six-phase induction motor drives," *IEEE Trans. Ind. Electron.*, vol. 68, no. 5, pp. 3672–3682, May 2021.

[3] A. S. Abdel-Khalik, A. M. Massoud, and S. Ahmed, "Effect of DC-link voltage limitation on postfault steady-state performance of asymmetrical six-phase induction machines," *IEEE Trans. Ind. Electron.*, vol. 65, no. 9, pp. 6890–6900, Sep. 2018.

[4] M. K. Pinjala and R. Bhimasingu, "Improving the DC-link utilization of nine-switch boost inverter suitable for six-phase induction motor," *IEEE Trans. Transport. Electrific.*, vol. 6, no. 3, pp. 1177–1187, Sep. 2020.

[5] M. J. Duran, E. Levi, and F. Barrero, "Multiphase electric drives: Introduction," *Wiley Encyclopedia Electr. Electron. Eng.*, pp. 1–26, Dec. 2017. [Online]. Available: https://onlinelibrary.wiley.com/doi/10.1002/047134608X.W8364

[6] A. Salem and M. Narimani, "A review on multiphase drives for automotive traction applications," *IEEE Trans. Transport. Electrific.*, vol. 5, no. 4, pp. 1329–1348, Dec. 2019.

[7] A. Pantea, A. Yazidi, F. Betin, S. Carriere, A. Sivert, B. Vacossin, H. Henao, and G.-A. Capolino, "Fault-tolerant control of a low-speed six-phase induction generator for wind turbines," *IEEE Trans. Ind. Appl.*, vol. 55, no. 1, pp. 426–436, Jan. 2019.

[8] C. Hou, M. Zhu, Z. Li, Y. Li, and X. Cai, "Inter harmonic THD amplification of voltage source converter: Concept and case study," *IEEE Trans. Power Electron.*, vol. 35, no. 12, pp. 12651–12656, Dec. 2020.

[9] Y. Kali, M. Ayala, J. Rodas, M. Saad, J. Doval-Gandoy, R. Gregor, and K. Benjelloun, "Time delay estimation based discrete-time super-twisting current control for a six-phase induction motor," *IEEE Trans. Power Electron.*, vol. 35, no. 11, pp. 12570–12580, Nov. 2020.

[10] S. Toledo, E. Maqueda, M. Rivera, R. Gregor, P. Wheeler, and C. Romero, "Improved predictive control in multi-modular matrix converter for six-phase generation systems," *Energies*, vol. 13, no. 10, p. 2660, May 2020.

[11] P. Szczepankowski, P. Wheeler, and T. Bajdecki, "Application of analytic signal and smooth interpolation in pulsewidth modulation for conventional matrix converters," *IEEE Trans. Ind. Electron.*, vol. 67, no. 12, pp. 10011–10023, Dec. 2020.

[12] W. Deng, H. Li, and J. Rong, "A novel direct torque control of matrix converter-fed PMSM drives using dynamic sector boundary for common-mode voltage minimization," *IEEE Trans. Ind. Electron.*, vol. 68, no. 1, pp. 70–80, Jan. 2021.

[13] M. Vijayagopal, C. Silva, L. Empringham, and L. de Lillo, "Direct predictive current-error vector control for a direct matrix converter," *IEEE Trans. Power Electron.*, vol. 34, no. 2, pp. 1925–1935, Feb. 2019.

[14] S. Toledo, D. Gregor, E. Maqueda, J. Rodas, M. Rivera, R. Gregor, F. Gavilan, and D. Caballero, "Multi-modular matrix converter topology applied to distributed generation systems," in *Proc. 8th IET Int. Conf. Power Electron., Mach. Drives (PEMD)*, Apr. 2016, pp. 1–6.

[15] S. Toledo, M. Rivera, R. Gregor, J. Rodas, and L. Comparatore, "Predictive current control with reactive power minimization in six-phase wind energy generator using multi-modular direct matrix converter," in *Proc. IEEE ANDESCON*, Oct. 2016, pp. 1–4.

[16] S. Toledo, M. Ayala, R. Gregor, A. Renault, M. Rivera, T. Dragicevic, and P. Wheeler, "Active and reactive power control based on predictive voltage control in a six-phase generation system using modular matrix converters," in *Proc. IEEE Int. Conf. Ind. Technol. (ICIT)*, Feb. 2020, pp. 1059–1065.

[17] S. M. A. Cruz, G. D. Marques, P. F. C. Goncalves, and M. F. Iacchetti, "Predictive torque and rotor flux control of a DFIG-DC system for torque ripple compensation and loss minimization," *IEEE Trans. Ind. Electron.*, vol. 65, no. 12, pp. 9301–9310, Dec. 2018.

[18] L. Yan and X. Song, "Design and implementation of Luenberger model-based predictive torque control of induction machine for robustness improvement," *IEEE Trans. Power Electron.*, vol. 35, no. 3, pp. 2257–2262, Mar. 2020.

[19] I. Gonzalez-Prieto, M. J. Duran, J. J. Aciego, C. Martin, and F. Barrero, "Model predictive control of six-phase induction motor drives using virtual voltage vectors," *IEEE Trans. Ind. Electron.*, vol. 65, no. 1, pp. 27–37, Jan. 2018.

[20] P. Gonçalves, S. Cruz, and A. Mendes, "Finite control set model predictive control of six-phase asymmetrical machines—An overview," *Energies*, vol. 12, no. 24, p. 4693, Dec. 2019.

[21] M. Siami, D. A. Khaburi, M. Rivera, and J. Rodríguez, "An experimental evaluation of predictive current control and predictive torque control for a PMSM fed by a matrix converter," *IEEE Trans. Ind. Electron.*, vol. 64, no. 11, pp. 8459–8471, Nov. 2017.

[22] R. Vargas, J. Rodriguez, C. A. Rojas, and M. Rivera, "Predictive control of an induction machine fed by a matrix converter with increased efficiency and reduced common-mode voltage," *IEEE Trans. Energy Convers.*, vol. 29, no. 2, pp. 473–485, Jun. 2014.

[23] G. Gontijo, M. Soares, T. Tricarico, R. Dias, M. Aredes, and J. Guerrero, "Direct matrix converter topologies with model predictive current control applied as power interfaces in AC, DC, and hybrid microgrids in islanded and grid-connected modes," *Energies*, vol. 12, no. 17, p. 3302, Aug. 2019.

[24] J. Zhang, M. Norambuena, L. Li, D. Dorrell, and J. Rodriguez, "Sequential model predictive control of three-phase direct matrix converter," *Energies*, vol. 12, no. 2, p. 214, Jan. 2019.

[25] J. Rodas, I. Gonzalez-Prieto, Y. Kali, M. Saad, and J. Doval-Gandoy, "Recent advances in model predictive and sliding mode current control techniques of multiphase induction machines," *Frontiers Energy Res.*, vol. 9, p. 445, Aug. 2021.

[26] M. J. Duran, I. Gonzalez-Prieto, F. Barrero, E. Levi, L. Zarri, and M. Mengoni, "A simple braking method for six-phase induction motor drives with unidirectional power flow in the base-speed region," *IEEE Trans. Ind. Electron.*, vol. 64, no. 8, pp. 6032–6041, Aug. 2017.

[27] M. Ayala, J. Rodas, R. Gregor, J. Doval-Gandoy, O. Gonzalez, M. Saad, and M. Rivera, "Comparative study of predictive control strategies at fixed switching frequency for an asymmetrical six-phase induction motor drive," in *Proc. IEEE Int. Electr. Mach. Drives Conf. (IEMDC)*, May 2017, pp. 1–8.

[28] F. Wang, Z. Zhang, X. Mei, J. Rodríguez, and R. Kennel, "Advanced control strategies of induction machine: Field oriented control, direct torque control and model predictive control," *Energies*, vol. 11, no. 1, p. 120, Jan. 2018.

[29] J. Rodriguez, C. Garcia, A. Mora, A. Davari, J. Rodas, D. F. V. Garcia, M. F. Elmorshedy, F. Wang, K. Zuo, L. Tarisciotti, and F. Flores-Bahamonde, "Latest advances of model predictive control in electrical drives—Part II: Applications and benchmarking with classical control methods," *IEEE Trans. Power Electron.*, early access, Oct. 20, 2021, doi: 10.1109/TPEL.2021.3121589.

[30] M. Khosravi, M. Amirbande, D. A. Khaburi, M. Rivera, J. Riveros, J. Rodriguez, A. Vahedi, and P. Wheeler, "Review of model predictive control strategies for matrix converters," *IET Power Electron.*, vol. 12, no. 12, pp. 3021–3032, Oct. 2019.

[31] E. Gary, A. Magno, and R. Jorge, "Design, analysis and validation of a six-phase induction machine from a commercial three-phase for academic research," *IEEE Latin Amer. Trans.*, vol. 18, no. 11, pp. 1943–1952, Nov. 2020.

[32] A. Olloqui, J. L. Elizondo, M. Rivera, M. E. Macias, O. M. Micheloud, R. Pena, and P. Wheeler, "Model-based predictive rotor current control strategy for indirect power control of a DFIM driven by an indirect matrix converter," *IEEE Trans. Energy Convers.*, vol. 36, no. 2, pp. 1510–1516, Jun. 2021.

EDGAR MAQUEDA was born in San Lorenzo, Paraguay, in 1989. He received the degree in electronics engineering with emphasis in industrial control from the Polytechnic Faculty, National University of Asuncion (UNA), San Lorenzo, in 2014, and the M.Sc. degree in electronics engineering with emphasis in power electronics from the Faculty of Engineering, UNA, in 2017. He is currently a Researcher with the Laboratory of Power Systems and Control (LSPyC), Faculty of Engineering, UNA. His work focuses on the development of new power converters applied to distributed energy generation using renewable sources.

SERGIO TOLEDO (Member, IEEE) was born in Luque, Paraguay, in 1985. He received the B.Eng. degree in electronic engineering from the Universidad Nacional de Asunción, Paraguay, in 2011, and the M.Sc. degree from the Centro de Investigación Científica y Educación Superior de Ensenada, México, in 2014. He is currently pursuing the Ph.D. degree with the Universidad de Talca, Chile. He is also an Associate Professor with the Universidad Nacional de Asunción. His main research interests include power electronics, control systems, matrix converters, and distributed generation systems. He is an active member of the Industrial Electronics Society (IES) and was awarded with the Best Conference Paper Award of the IES in 2021.

DAVID CABALLERO was born in Luque, Paraguay, in 1987. He received the bachelor's and M.Sc. degrees in electronic engineering from the Universidad Nacional de Asunción (UNA), in 2014 and 2017, respectively, where he is currently pursuing the Ph.D. degree in electronics engineering. He participated in several national and international events as a presenter and carried out research stays at the University of Talca, Chile, in 2016, 2017, and 2020. He is also a Professor in

control systems and electronics, and the Head of the University Extension Department, FIUNA. His research interest includes the design and implementation of discrete time control strategies for power converter applications. In 2016, his research work on control of matrix converters was awarded as the Best Paper at the WMSCI International Conference.

FEDERICO GAVILAN was born in Asuncion, Paraguay, in 1987. He received the M.Sc. degree in electronic engineering with an emphasis on power electronics from the Faculty of Engineering, National University of Asuncion (UNA), San Lorenzo, Paraguay, in 2017, where he is currently pursuing the Doctoral degree in engineering with an emphasis on power electronics. He began as a Research Professor with the Laboratory of Power and Control Systems, Faculty of Engineering, UNA, in 2015. His works were focused on the development of predictive control algorithms applied to power converters in the generation of distributed energy using renewable sources. He was a Teacher of four subjects. He received the title of Electronic Engineer from the Faculty of Engineering, UNA, in 2014. He was the Winner of the Pujol Awards for the Best Assistant and the Best Professor.

JORGE RODAS (Senior Member, IEEE) was born in Asunción, Paraguay, in 1984. He received the B.Eng. degree in electronic engineering from the Universidad Nacional de Asunción (UNA), Paraguay, in 2009, the M.Sc. degree from the Universidad de Vigo, Spain, in 2012, the M.Sc. degree from the Universidad de Sevilla, Spain, in 2013, and the joint-university Ph.D. degree from the Universidad Nacional de Asunción and the Universidad de Sevilla, in 2016.

In 2011, he joined the Laboratory of Power and Control Systems (LSPyC), Faculty of Engineering, UNA, where he currently serves as a Professor. In 2017, he made a research stay at the Power Electronics and Industrial Control Research Group, École de Technologie Supérieure, Montreal, Canada. His research interests include applications of advanced control to real-world problems. His current research activities include applying model-based predictive control and nonlinear control to power electronic converters, renewable energy conversion systems, electric motor drives, and robotic systems (especially drones).

Prof. Rodas received the Paraguayan National Science Award in 2020. He served as a Guest Editor for *Energies* (MDPI). He also serves as an Associate Editor for *Alexandria Engineering Journal* (Elsevier), and a Guest Editor for the *World Electric Vehicle Journal* (MDPI) and *Frontiers in Energy Research*.

MAGNO AYALA received the B.Eng. degree in electronic engineering from the Universidad Nacional de Asunción (UNA), Paraguay, in 2014, and the M.Sc. and Ph.D. degrees in power electronics from the Engineering Faculty, UNA, in 2017 and 2020, respectively. He joined the Laboratory of Power and Control System, UNA, in 2015, working as a Research Assistant. His research interest includes control of multiphase ac machines.

LARIZZA DELORME (Student Member, IEEE) was born in Asuncion, Paraguay, in 1990. She received the B.Eng. degree in electronic engineering with an emphasis in industrial control from the Universidad Nacional de Asuncion (UNA), Paraguay, in 2017, and the M.Sc. degree in electronic engineering with an emphasis on renewable energies and energy efficiency from the Universidad del Cono Sur de las Americas, in 2020. She is currently working as a Research Assistant with the Laboratory of Power and Control System (LSPyC), UNA. Her research interests include modelling, simulation, and control of multiphase drives.

RAUL GREGOR was born in Asunción, Paraguay, in 1979. He received the B.Eng. degree in electronic engineering from the Catholic University of Asunción, Paraguay, in 2005, and the M.Sc. and Ph.D. degrees in electronics, signal processing, and communications from the Higher Technical School of Engineering (ETSI), University of Seville, Spain, in 2008 and 2010, respectively. Since March 2010, he has been the Head of the Laboratory of Power and Control Systems (LSPyC), Engineering Faculty, National University of Asunción (FIUNA), Paraguay, where he is currently the Head of the Department of Electronic and Mechatronics Engineering. He has authored or coauthored about 150 technical journals in the field of power electronics and control systems. His research interests include multiphase drives; advanced control of power converter topologies; power quality; renewable energies; modeling, simulation, optimization, and control of power systems; smart metering and smart grids; and predictive control. He received the Best Paper Award from the IEEE Transactions on Industrial Electronics, Industrial Electronics Society, in 2010; and the Best Paper Award from the *IET Electric Power Applications*, in 2012.

MARCO RIVERA (Senior Member, IEEE) received the B.Sc. degree in electronics engineering and the M.Sc. degree in electrical engineering from the Universidad de Concepción, Chile, in 2007 and 2008, respectively, and the Ph.D. degree from the Department of Electronics Engineering, Universidad Técnica Federico Santa María, Valparaíso, Chile, in 2011. From 2011 to 2012, he was working as a Postdoctoral Researcher and a part-time Professor with the Department of Electronics Engineering, Universidad Técnica Federico Santa María. He is currently a Full Professor with the Department of Electrical Engineering, Universidad de Talca, Curicó, Chile. His research interests include matrix converters, predictive and digital controls for high-power drives, and four-leg converters. In 2013, he was awarded the Premio Tesis de Doctorado Academia Chilena de Ciencias 2012, which was awarded to the Best Ph.D. Thesis developed in 2011 for national and foreign students in any exact or natural sciences program, that is a member of the Academia Chilena de Ciencias, Chile. In 2015, he was awarded the Outstanding Engineer of 2015 by the Chilean Association of Electrical and Electronics Industry and the IEEE-Chile. In 2021, he was awarded the 2021 Best Conference Paper Award of the IEEE Industrial Electronics Society (IES). He received the Scholarship from the Chilean Research Fund CONICYT for his Ph.D.

● ● ●